PERGAMON

International Journal of Solids and Structures 36 (1999) 4941–4962

INTERNATIONAL JOURNAL OF SOLIDS and STRUCTURES

Comparison of different implementation algorithms for HiSS constitutive models in FEM

G.W. Wathugala*, S. Pal

Department of Civil and Environmental Engineering, Louisiana State University, Baton Rouge, LA 70803, U.S.A.

Received 13 August 1997; accepted 20 July 1998

Abstract

Relative accuracy, stability and efficiency of four popular algorithms to implement elasto-plastic constitutive models in non-linear finite element procedures have been compared. Elastic Predictor–Plastic Corrector (EP–PC) method, Plastic Predictor–Plastic Corrector (PP–PC) method, Implicit Integration (Implicit) method and Modified Euler (ME) method were used to implement Hierarchical Single Surface (HiSS) δ_0^* model into the general purpose finite element program ABAQUS. First, these algorithms were used outside the finite element program to simulate various triaxial stress paths. After that, they were used in ABAQUS to simulate two strip footings: (a) displacement controlled rigid footing and (b) load controlled flexible footing. The effect of the sub-strain increment size on the accuracy, stability and efficiency of each algorithm during these simulations have been compared. Implicit Method and ME performed well for some problems but performed poorly on others. EP–PC and PP–PC methods performed equally well for all the problems. This also showed the importance of testing algorithms under various stress paths and boundary value problems to assess their relative performance.

1. Introduction

The stress–strain behavior of soils is nonlinear and stress and strain paths dependent. Unlike metals, many soils develop volumetric strains due to pure shear stresses. These characteristics of soils make all the advanced constitutive models developed for them very complex. The complexity of these constitutive models prevents development of analytical solutions for boundary value problems. To be useful in solving practical problems, these models need to be implemented into numerical solution techniques. Thus, developing efficient and robust algorithms for implementation of constitutive models in computer procedures is very important.

There are several types of algorithms used to implement plasticity based constitutive models in FEM. Even though there are many papers on individual algorithms, systematic comparisons of

* Corresponding author

0020-7683/99/$ - see front matter
PII: S0020-7683(98)00273-X

the performance of different types of algorithms are rare. In this paper, the relative performance of four algorithms in predicting stress and strain controlled laboratory tests and load and displacement controlled boundary value problems has been compared. The four algorithms used here can be classified as (1) elastic-predictor–plastic corrector (EP–PC); (2) plastic-predictor–plastic corrector (PP–PC); (3) Implicit Integration (Implicit); and (4) modified Euler (ME). All these algorithms were implemented in the commercial finite element program ABAQUS (HKS Inc., 1996) and used for all the boundary value problems presented here. Based on the numerical tests, it was concluded that EP–PC and PP–PC performed equally and were better in all aspects, i.e., in terms of accuracy, stability and efficiency than other methods.

We have used the Hierarchical Single Surface (HiSS) δ_0^* model (Wathugala and Desai, 1993) in the numerical comparison. However, all the derivations were done for a general plasticity based model whenever possible. The concepts and ideas developed here may be applicable to other plasticity based models and especially other HiSS models. The HiSS δ_0^* model is the associative plasticity model developed for normally consolidated and overconsolidated clays. A brief description of the model is given below for completeness. For more details, readers are referred to Wathugala and Desai (1993) and Wathugala (1990).

2. HiSS δ_0^* constitutive model

The HiSS δ_0^* constitutive model is an elasto-plastic constitutive model, but it allows nonlinear reloading (RL). The virgin loading (VL) has been modelled in the framework of plasticity theory, and the yield surface F is defined in terms of stress invariants, the first invariant of the stress tensor, J_1, the second invariant of the deviatoric stress tensor, J_{2D}, and the third invariant of the deviatoric stress tensor, J_{3D}, as

$$F \equiv \left(\frac{J_{2D}}{p_a^1}\right) - \left[-\alpha_{ps}\left(\frac{J_1}{p_a}\right)^n + \gamma\left(\frac{J_1}{p_a}\right)^2 \right](1-\beta S_r)^{-0.5} = 0 \tag{1}$$

where p_a is the atmospheric pressure, and α_{ps} is the hardening or growth function space. γ, β and n are material parameters. S_r is defined as a stress ratio, and given by

$$S_r \equiv \frac{\sqrt{27}}{2} J_{3D} J_{2D}^{-3/2}.$$

The shape of the yield surface for a typical soil in different stress spaces is shown in Figs 1 and 2. When $\alpha_{ps} = 0$, the yield surface becomes the ultimate surface, which envelops all the yield surfaces.

The hardening function for the δ_0^* model is defined as:

$$\alpha_{ps} = \frac{h_1}{(\xi_v + h_3 \xi_D^{h_4})^{h_2}} \tag{2}$$

where h_1, h_2, h_3 and h_4 are material parameters. For clays, making h_3 equal to zero yields the intended contractive response. In that case, eqn 2 simplifies to a volumetric hardening function. The increments of trajectories of total, volumetric, and deviatoric plastic strains (ξ_v and ξ_D) are defined here as:

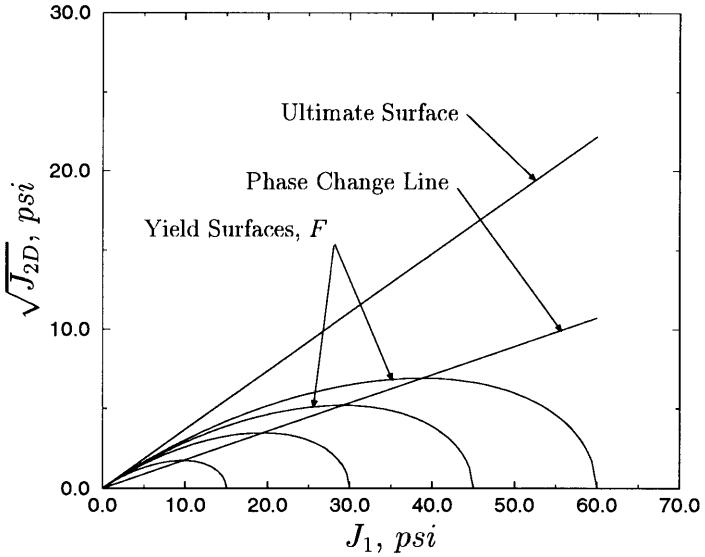

Fig. 1. Shape of yield surfaces in $J_1 - \sqrt{J_{2D}}$ plane.

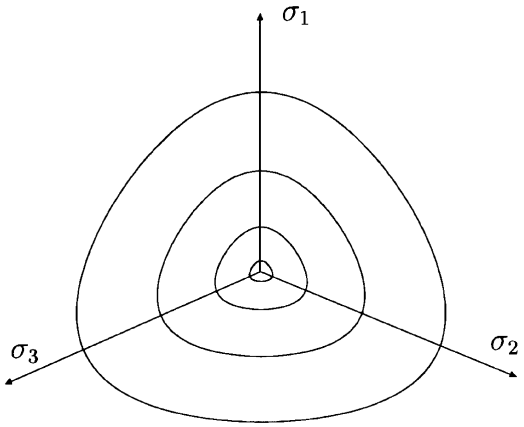

Fig. 2. Shape of yield surfaces in octahedral plane.

$$\mathrm{d}\xi = (\mathrm{d}\varepsilon_{ij}^{p}\,\mathrm{d}\varepsilon_{ij}^{p})^{\frac{1}{2}}, \quad \mathrm{d}\xi_D = (\mathrm{d}\varepsilon_{ij}^{p}\,\mathrm{d}\varepsilon_{ij}^{p})^{\frac{1}{2}} \quad \text{and} \quad \mathrm{d}\xi_v = \frac{1}{\sqrt{3}}\langle \mathrm{d}\varepsilon_v^{p} \rangle;$$

$\mathrm{d}\varepsilon_{ij}^{p}$ is the incremental deviatoric plastic strain tensor; $\mathrm{d}\varepsilon_v^{p}$ is the incremental volumetric plastic strain due to virgin loading.

$\langle\,\rangle$ are McAuley brackets and $\langle \mathrm{d}\varepsilon_v \rangle = \mathrm{d}\varepsilon_v$ for $\mathrm{d}\varepsilon_v > 0$, and $\langle \mathrm{d}\varepsilon_v \rangle = 0$ for $\mathrm{d}\varepsilon_v \leqslant 0$.

3. Incremental stress–strain relationship

The incremental stress–strain relationship for virgin loading is given by

$$d\sigma_{ij} = C^{VL}_{ijkl}\, d\varepsilon_{kl} \tag{3}$$

where C^{VL}_{ijkl} is the elasto-plastic constitutive stiffness tensor for virgin loading. General form of C^{VL}_{ijkl} is given by Wathugala (1990) as

$$C^{VL}_{ijkl} = C^{e}_{ijkl} - \frac{C^{e}_{ijnm} n^{F}_{nm} n^{F}_{op} C^{e}_{opkl}}{H^{VL} + n^{F}_{rs} C^{e}_{rstu} n^{F}_{tu}} \tag{4}$$

where C^{e}_{ijkl} is the elastic constitutive stiffness tensor. The tensor n^{F}_{ij} is defined as the unit normal tensor to the yield surface, and H^{VL} is the virgin plastic modulus. It is found from the consistency condition in the theory of plasticity as

$$H^{VL} = -\frac{\dfrac{\partial F}{\partial \alpha_{ps}}}{\left[\dfrac{\partial F}{\partial \sigma_{mn}} \dfrac{\partial F}{\partial [gksl]_{mn}}\right]^{1/2}} \frac{\partial \alpha_{ps}}{\partial \xi_D} (n^{F}_{Dij} n^{F}_{Dij})^{1/2} + \frac{\partial \alpha_{ps}}{\partial \xi_v} \frac{\langle n^{F}_{kk} \rangle}{\sqrt{3}} \tag{5}$$

where n^{F}_{Dij} is the deviatoric part of the n^{F}_{ij} tensor.

3.1. Non-virgin loading

In the HiSS δ^{*}_{0} model, non-virgin loadings are further divided into unloading and reloading depending on whether stress increment is directed outward or inward to the reference surface, R. The shape of R is similar to that of the F surface and can be obtained by replacing α_{ps} in eqn 1 with α_r. The value of α_r is obtained by equating $R = 0$ and substituting current stresses. The unloading is assumed to be linear elastic. The nonlinear incremental stress-strain relation for reloading has been developed similar to that for the virgin loading with the following modifications: (a) by substituting n^{F}_{ij} by n^{R}_{ij}, which is the unit normal tensor for the reference surface R; (b) plastic modulus for virgin loading H^{VL} is replaced by the plastic modulus for reloading H^{RL} which is found from an interpolation function given below.

$$H^{RL} = H^{VL}_{I_1} + H^{VL}_{I_2} r_1 \left(1 - \frac{\alpha_{ps}}{\alpha_r}\right)^{r_2} \tag{6}$$

where r_1 and r_2 are material parameters, and $H^{VL}_{I_1}$ and $H^{VL}_{I_2}$ are virgin plastic moduli at points I_1 and I_2 on the prestress surface (Fig. 3). The image point I_1 is located at the intersection between the radial line passing through the current stress and the prestress surface. The point I_2 is located at the intersection of the hydrostatic compression line and the prestress surface.

4. Strain to stress algorithm

Displacement based nonlinear FEM procedures require a module which provides the stress increment corresponding to a given strain increment for each Gauss integration point in each

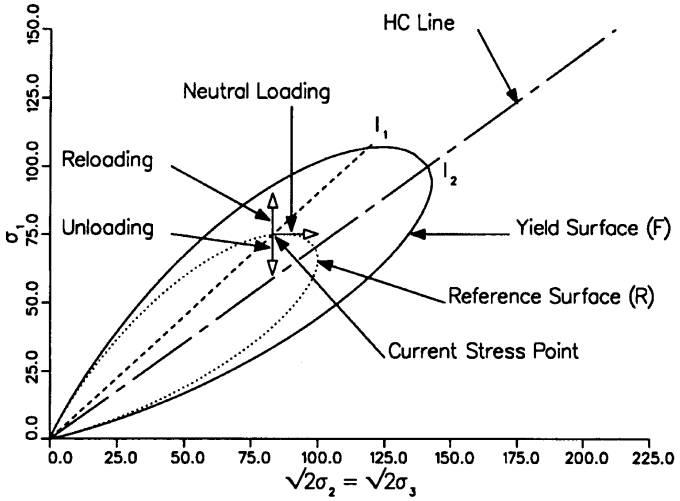

Fig. 3. Yield surface and reference surface in triaxial plane.

element for each Newton Raphson (NR) or Modified NR iteration. The strain to stress algorithms presented here are used to develop this module. In realistic boundary value problems, the strain path followed by Gauss integration points can be complex. The size of the strain increment can also vary widely. Therefore, it is important that these algorithms should be very stable and accurate for variety of strain paths and for large strain increments. Since this module is called so many times during a single analysis, computational efficiency of this module can dominate the overall efficiency of the FEM procedure or program.

Normally, the FEM program provides the strain increment, current stress and history parameters to the constitutive model module. The first step in the algorithm is to determine the location of the current stress point with respect to the current yield surface. It could be inside or on the yield surface. According to the theory of plasticity, it is not possible to have the stress point outside the yield surface. If the stress point is found to be outside the yield surface, then that is due to numerical errors, and it should be moved back to the yield surface by correcting the stress point or yield surface or both. Traditionally, the location of the current stress (σ_{ij}) point is found by evaluating the yield function, F. If the stress point is on the yield surface, $F(\sigma_{ij}, \alpha_{ps}) = 0$, and if it is inside, $F(\sigma_{ij}, \alpha_{ps}) < 0$.

The second step is to determine the direction of the stress increment. The exact direction of the stress increment, $d\sigma_{ij}$, for a given strain increment, $d\varepsilon_{kl}$, is not known in advance. Therefore an approximate direction is evaluated by assuming elastic behavior. This stress increment is commonly known as the elastic predictor stress increment, $d\sigma^e_{ij}$. It may be calculated from

$$d\sigma^e_{ij} = C^e_{ijkl}\, d\varepsilon_{kl}. \tag{7}$$

The possible elastic predictor stress increment directions when the stress point is inside the yield surface is shown in Fig. 4. It should be noted here that the correct stress increment directions for loading cases are different from the elastic predictor directions. However, the constitutive model is formulated in such a way that when the elastic predictor indicates loading, the correct stress

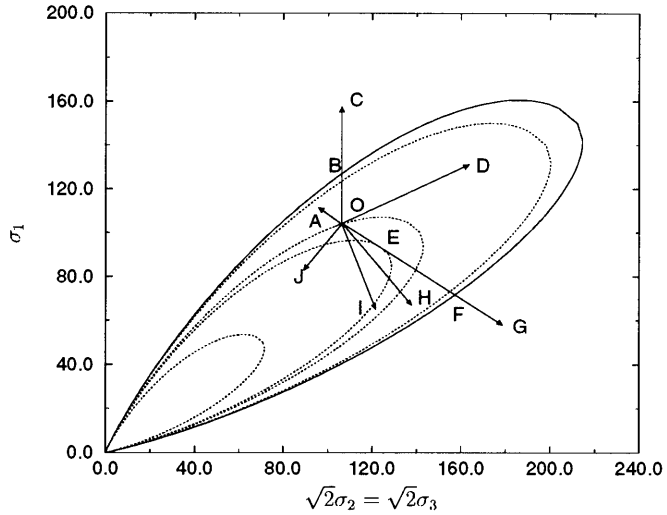

Fig. 4. Possible stress increment directions when current stress is inside the yield surface (after Wathugala, 1990).

Table 1
Possible stress increment directions when the current stress is inside the yield surface (after Wathugala, 1990)

Stress increment	$d\sigma_{ij}^e n_{ij}^F$	$F(\sigma_{ij}^e, \alpha_{ps})$	α_r^e	Description
OA	>0	<0	$\alpha_r > \alpha_r^e > 0$	Reloading
OB	>0	$=0$	$\alpha_r > \alpha_r^e = 0$	Reloading
OC	>0	>0	$\alpha_r > \alpha_{ps} > 0$	Reloading followed by Virgin Loading
OD	$=0$	<0	$\alpha_r > \alpha_r^e > 0$	Neutral Loading followed by Reloading
OE, OJ	<0	<0	$\alpha_r^e > \alpha_r > 0$	Unloading
OF	<0	$=0$	$\alpha_r > \alpha_r^e = 0$	Unloading followed by Reloading
OG	<0	>0	$\alpha_r > \alpha_{ps} > 0$	Unloading followed by Reloading and Virgin Loading
OH	<0	<0	$\alpha_r > \alpha_r^e > 0$	Unloading followed by Reloading
OI	<0	<0	$\alpha_r^e > \alpha_r > 0$	Unloading followed by Reloading

direction is also directed outwards to the reference surface (yield surface for the virgin loading case). Some properties of these elastic predictors are given in Table 1. Details of algorithms used to identify each part of the stress path are given in Wathugala (1990) and Pal (1997). The same algorithm for the non-virgin loading is used in all the analyses.

4.1. Virgin loading

In general, the incremental stress, $d\sigma_{ij}$, corresponding to a given strain increment, $d\varepsilon_{ij}$, may be found from eqn 3. However, C_{ijkl}^{VL} changes with σ_{ij} and hardening parameters that are related to the plastic strains. If eqn 3 is used repeatedly, linearizing errors get accumulated and the stress point

starts to drift away from the yield surface. Four algorithms described here use different techniques to achieve accurate integration of the constitutive relationship for virgin loadings. Modified Euler method limits linearizing error by adjusting the size of the substep, whereas other methods use iterative schemes to correct the errors in each step before moving to the next step.

The basic problem in calculating stress increment, $d\sigma_{ij}$ corresponding to a given strain increment, $d\varepsilon_{kl}$ which causes virgin loading, may be expressed as follows:

given: σ_{ij}^{O}, α_{ps}^{O}, ξ_i^{O}, $d\varepsilon_{kl}$ and $F(\sigma_{ij}^{O}, \alpha_{ps}^{O}) = 0$
find: σ_{ij}^{C} and α_{ps}^{C} so that $F(\sigma_{ij}^{C}, \alpha_{ps}^{C}) = 0$
where: σ_{ij}^{C} and α_{ps}^{C} are found from $d\varepsilon_{kl} = d\varepsilon_{kl}^{e} + d\varepsilon_{kl}^{p}$, $d\sigma_{ij} = C_{ijkl}^{e} d\varepsilon_{kl}^{e}$, $\sigma_{ij}^{C} = \sigma_{ij}^{O} + d\sigma_{ij}$, $d\xi_i = f_i(d\varepsilon_{kl}^{p})$, $\xi_i^{C} = \xi_i^{O} + d\xi_i$, and $\alpha_{ps}^{C} = f_{\alpha}(\xi_i^{C})$.

Here, superscripts O and C refer to initial and final converged quantities. F is the yield function, and f_{α} is the hardening function. Total, elastic, and plastic strain increments are given by $d\varepsilon_{kl}$, $d\varepsilon_{kl}^{e}$, and $d\varepsilon_{kl}^{p}$ respectively. C_{ijkl}^{e} is the elastic constitutive tensor, and ξ_i are different trajectories of plastic strains such as ξ, ξ_D and ξ_V. The functions, f_i, relate incremental plastic strains to incremental trajectories. Plastic strain in this step should also conform to the flow rule ($d\varepsilon_{kl}^{p} = \lambda n_{kl}^{O}$, where n_{kl}^{O} is the direction of plastic strain). If the exact decomposition of the incremental strain tensor, $d\varepsilon_{kl}$, into its elastic and plastic components is known, σ_{ij}^{C}, ξ_i^{C} and α_{ps}^{C} can be computed. Unfortunately, this decomposition of the incremental strain tensor is not known in advance, and most of the iterative schemes for solution of the above system start with a trial decomposition of the incremental strain tensor.

4.2. Predictor–corrector type algorithms

Elastic Predictor–Plastic Corrector (EP–PC) and Plastic Predictor–Plastic Corrector (PP–PC) methods presented here were developed by modifying and improving algorithms by Ortiz and Simo (1986) and Potts and Gens (1985), respectively. However, they are very similar and therefore both the methods are described together here. The differences will be indicated at appropriate locations in the derivation.

All the methods in this group start with a trial decomposition of the incremental strain tensor. Let us assume that these trial solutions move stress to an intermediate state I, and a single correction moves it to the final converged solution at C. This is schematically illustrated in Fig. 5.

If the trial solution assumes the decomposition for the strain tensor to be

$$d\varepsilon_{kl} = d\varepsilon_{kl}^{e,OI} + d\varepsilon_{kl}^{p,OI} \tag{8}$$

then all the quantities at the intermediate state, I, can be computed. If point C is on the yield surface,

$$F(\sigma_{ij}^{I} + d\sigma_{ij}^{IC}, f_{\alpha}(\xi_i^{I} + d\xi_i^{IC})) = 0 \tag{9}$$

Taylor's series expansion of eqn 9 around the point I is given by

$$0 = F(\sigma_{ij}^{I}, f_{\alpha}(\xi_i^{I})) + \left[\frac{\partial f}{\partial \sigma_{ij}}\right]_I d\sigma_{ij}^{IC} + \left[\frac{\partial F}{\partial \alpha_{ps}} \frac{\partial f_{\alpha}}{\partial \xi_i}\right]_I d\xi_i^{IC} + \text{higher order terms.} \tag{10}$$

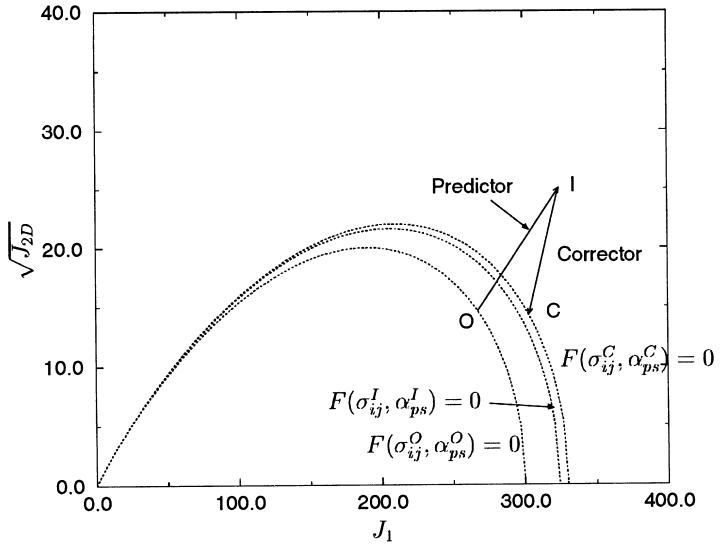

Fig. 5. Schematic diagram for ideal predictor corrector algorithm (after Wathugala, 1990).

By using flow rule, $d\varepsilon_{kl}^{p,IC} = d\lambda^{IC} n_{kl}^O$, for most of the constitutive models in practice, $d\sigma_{ij}^{IC}$ and $d\xi_i^{IC}$ can be expressed in terms of the single variable, $d\lambda^{IC}$ as

$$0 = F(\sigma_{ij}^I, f_\alpha(\xi_i^I)) + \left\{ \left[\frac{\partial f}{\partial \sigma_{ij}} \right]_I C_{ijkl}^e n_{kl}^O + \left[\frac{\partial F}{\partial \alpha_{ps}} \frac{\partial f_\alpha}{\partial \xi_i} \right]_I f_i(n_{kl}^O) \right\} d\lambda^{IC} + \text{higher order terms of } d\lambda^{IC}. \tag{11}$$

By neglecting higher order terms of $d\lambda^{IC}$, eqn 11 may be solved for $d\lambda^{IC}$ as

$$d\lambda^{IC} = \frac{-F(\sigma_{ij}^I, f_\alpha(\xi_i^I))}{\left\{ \left[\frac{\partial f}{\partial \sigma_{ij}} \right]_I C_{ijkl}^e n_{kl}^O + \left[\frac{\partial F}{\partial \alpha_{ps}} \frac{\partial f_\alpha}{\partial \xi_i} \right]_I f_i(n_{kl}^O) \right\}}. \tag{12}$$

Now all the quantities at C can be computed. Since higher order terms in eqn 11 have been neglected, the solution obtained here would not satisfy the yield function given by eqn 1. The quantities obtained here actually refer to an intermediate state closer to the final converged solution. Substituting the solution obtained here as the intermediate state in eqn 12, the procedure is repeated until $d\lambda^{IC}$ or $F(\sigma_{ij}^I, \alpha_{ps}^I)$ is less than a prescribed tolerance.

4.3. Comparison of elastic predictor and plastic predictor methods

Two popular methods in evaluating the intermediate stress, (a) elastic predictor (b) plastic predictor, are compared here. In the EP–PC method, the initial $d\sigma_{ij}^{OI}$ is obtained by $C_{ijkl}^e d\varepsilon_{kl}$, while in the plastic predictor-plastic corrector method, it is calculated using elasto-plastic constitutive matrix, C_{ijkl}^{ep}, corresponding to the initial stress point O.

From eqn 12, σ_{ij}^{IC} may be expressed as

$$\sigma_{ij}^{IC} = \frac{-F(\sigma_{ij}^{I}, f_{\alpha}(\xi_i^{I}))C_{ijkl}^{e} n_{kl}^{Q}}{\left\{\left[\frac{\partial f}{\partial \sigma_{ij}}\right]_I C_{ijkl}^{e} n_{kl}^{Q} + \left[\frac{\partial F}{\partial \alpha_{ps}} \frac{\partial f_{\alpha}}{\partial \xi_i}\right]_I f_i(n_{kl}^{Q})\right\}}. \tag{13}$$

For the EP–PC method, $d\varepsilon_{kl}^{e,OI} = d\varepsilon_{kl}$ and $d\varepsilon_{kl}^{p,OI} = 0$. Therefore $\alpha_{ps}^{I} = \alpha_{ps}^{O}$. The yield function, F, at the point I may be expanded using the Taylor's series expansion around the point O as

$$F(\sigma_{ij}^{I}, \alpha_{ps}^{I}) = F(\sigma_{ij}^{O} + d\sigma_{ij}^{OI}, \alpha_{ps}^{O}) = F(\sigma_{ij}^{O} + \alpha_{ps}^{O}) + \left[\frac{\partial F}{\partial \sigma_{ij}}\right]_I d\sigma_{ij}^{OI} + \text{higher order terms.} \tag{14}$$

Since $d\varepsilon_{kl}^{e,OI} = d\varepsilon_{kl}$ for this method, $d\sigma_{ij}^{OI} = C_{ijkl}^{e} d\varepsilon_{kl}$. After some algebraic manipulations (Wathugala, 1990) an expression for $d\sigma_{ij}^{OC}$ may be found as

$$d\sigma_{ij}^{OC} = \left[C_{ijkl}^{e} + \frac{C_{ijrs}^{e} n_{rs}^{Q} \left(\frac{\partial F}{\partial \sigma_{mn}}\right)_O C_{mnkl}^{e}}{\left(\frac{\partial f}{\partial \sigma_{ij}}\right)_I C_{ijkl}^{e} n_{kl}^{Q} + \left(\frac{\partial F}{\partial \alpha_{ps}} \frac{\partial f_{\alpha}}{\partial \xi_i}\right)_I f_i(n_{kl}^{Q})} \right] d\varepsilon_{kl}. \tag{15}$$

The term inside the square bracket [] is similar to the expression for the C_{ijkl}^{ep} in eqn 4. The only difference is that all the terms in C_{ijkl}^{ep} are calculated at a single point, whereas in eqn 15, different terms are calculated at different points as indicated. In the drift correction method (Potts and Gens, 1985), C_{ijkl}^{ep} is calculated at the point O. For small strain increments, both methods give the same answer, but the elastic predictor method takes one more iteration to achieve the same accuracy. Since the elastic predictor method does not require the calculation of C_{ijkl}^{ep}, both methods require equal numerical effort to achieve the same convergence limits for small increments.

Wathugala (1990) and Pal (1997) have found that improved accuracy can be obtained by computing these quantities at a point closer to the point O. Using values at point O leads to numerical problems when stress path moves from pure hydrostatic to undrained shear. Any point close to point O would give good results. In the present study, all the quantities are computed at a point $0.1 \times OI$ away from the point O.

4.4. Implicit integration method

The implicit integration method used here is based on the Backward–Euler integration scheme where the normal to the potential surface, n_{kl}^{Q}, at the final stress state is used for the plastic correction. This method has been used by various researchers (Simo and Taylor, 1985; Borja and Lee, 1990; Jeremic and Sture, 1995; Macari et al., 1997; Pal, 1997) to integrate the elasto-plastic constitutive models.

The Backward–Euler integration scheme can be expressed as:

$$\sigma_{ij}^{C} = \sigma_{ij}^{I} - \lambda C_{ijkl}^{e} n_{kl}^{QC} \tag{16}$$

where σ_{ij}^{C} is the final stress state, σ_{ij}^{I} is the elastic prediction, and n_{kl}^{QC} is the normal to the plastic potential surface at the final stress state C. Generally, an initial estimate of σ_{ij}^{C} does not satisfy the

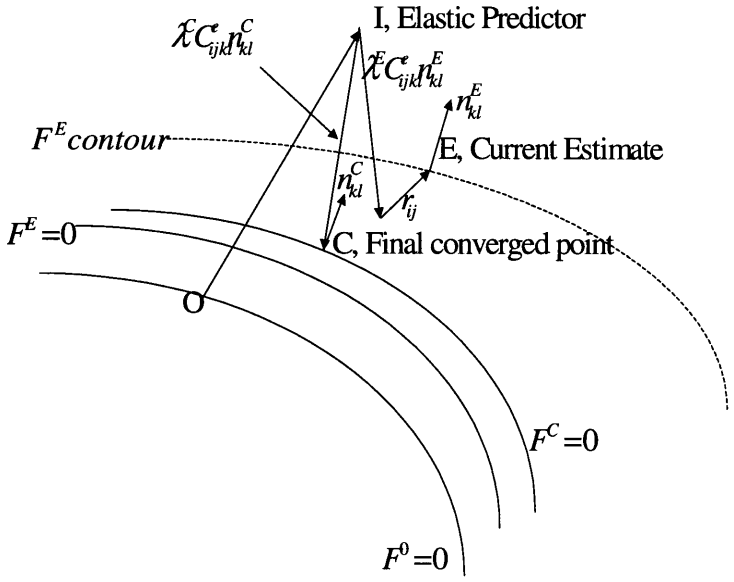

Fig. 6. Schematic representation of Implicit Method.

yield criteria as well as eqn 16 and an iterative scheme is necessary to bring the stress onto the yield surface.

In order to derive such an iterative scheme, a residual stress tensor is defined as:

$$r_{ij} = \sigma^C_{ij} - (\sigma^I_{ij} - \lambda C^e_{ijkl} n^{Q^C}_{kl}) \tag{17}$$

where r_{ij} represents the difference between estimated current state σ_{ij} (point E in Fig. 6) and the implicit stress state of Backward–Euler scheme ($\sigma^I_{ij} - \lambda C^e_{ijkl} n^Q_{kl}$), which represents the error in the current estimate of stress σ^C_{ij}. Equations 16 and 17 are schematically illustrated in Fig. 6. Due to space limitations, details of the algorithm are not given here. Readers are referred to Pal (1997) for more details.

4.5. Modified Euler method

Modified Euler scheme has been used by several researchers (Nayak and Zienkiewicz, 1972; Sloan, 1987; Ganendra and Potts, 1994; Pal, 1997) for integrating elasto-plastic constitutive models. Sloan (1987) modified the algorithm so that it controls the error in the integration of the constitutive model by adjusting the size of each substeps automatically. This method does not perform the drift correction generally used to make sure that the stress point lies on the yield surface. Therefore, this method can be used even with constitutive models that do not have yield surfaces. The detailed description of the method is given by Sloan (1987) and Pal (1997). A schematic representation of the Modified Euler method is shown in Fig. 7.

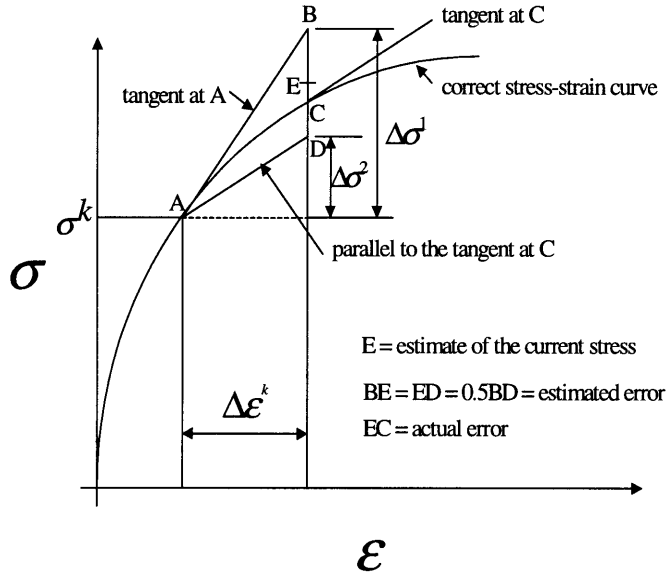

Fig. 7. Schematic representation of the Modified Euler method.

4.6. Subincrementation

All the four methods use subincrementation for better accuracy. In the Modified Euler method, the size of the subincrementation is controlled automatically depending on the accuracy of the solution (TOL value). The other methods, EP–PC, PP–PC, and Implicit, use fixed size subincrementation where the strain increment $d\varepsilon_{kl}$ is subdivided into n equal parts.

$$n = \text{largest integer part of} \left(\frac{d\varepsilon_{kl}}{\Delta\varepsilon_{\max}} \right) + 1 \tag{18}$$

where $\Delta\varepsilon_{\max}$ is the largest subincrement permitted. Now the subincrement strain, $\delta\varepsilon_{kl}$, may be calculated from $\delta\varepsilon_{kl} = d\varepsilon_{kl}/n$. For each subincrement strain, $\delta\varepsilon_{kl}$, the above mentioned algorithms are used to compute the stress increment $\delta\sigma_{ij}$. Assigning a large value for TOL in ME and $\Delta\varepsilon_{\max}$ in other methods will effectively stop subincrementation in these algorithms.

5. Comparing the performance of different algorithms

The overall performance of an algorithm may be studied by analyzing its accuracy, stability and efficiency. These aspects are related but they are different. Accuracy is defined as the ability to predict accurate results. Accuracy can be evaluated by comparing the numerical results from an algorithm with the 'exact' or a very accurate solution. Very accurate solutions may be obtained by (a) analytical solutions if and when available; (b) stress to strain algorithm (Wathugala and Desai, 1994); and (c) using an algorithm that converges to the exact answer for very small steps. The

ability of an algorithm to produce accurate results with large strain increments is desirable. Instability is defined here as the state where numerical results start varying randomly or start oscillating or inability to achieve convergence. Here, efficiency is defined as the inverse of the computing cost of achieving the same level of accuracy and stability. All three aspects discussed above are very important for an implementation algorithm.

The easiest way to analyse these algorithms is to input strain controlled paths directly into the model subroutines without connecting them to the finite element program. This allows better control of the program and facilitates interactive debugging and analyses. However, it is necessary to test these algorithms inside a finite element program during the solution of a real boundary value problem due to the following reason. At each global equilibrium iteration in nonlinear FEM, unbalanced loads are computed from the stresses provided by the constitutive model subroutine. The next strain increment supplied to the constitutive model subroutine at a Gauss integration point, is affected by the stresses at other Gauss integration points through the global equilibrium equations. Therefore, the stability of an integration algorithm outside a finite element program may be different from that during the solution of a real boundary value problem using FEM. In this study, we have compared all the algorithms for both cases described above. The results also showed that it is important to analyse these algorithms under different stress and strain paths before making a final conclusion of their performance. Material parameters for a typical clay have been used for all the analyses here ($E = 11{,}032$ kPa, $v = 0.35$, $\gamma = 0.047$, $\beta = 0$, $m = -0.5$, $n = 2.8$, $h_1 = 1.0 \times 10^{-4}$, $h_2 = 0.78$, $h_3 = 0$, and $h_4 = \text{NA}$). Since our objective is to compare the algorithms for virgin loading, all the numerical examples have been designed to experience virgin loading only. Therefore, non-virgin loading parameters do not affect our results. In the present study, linear elastic non-virgin loading has been assumed. However, the ideas presented in Fig. 4 and Table 1 for non-virgin loading are still necessary to improve the robustness of the algorithm (Wathugala and Pal, 1996).

5.1. Prediction of simulated triaxial tests

Three different triaxial tests have been selected so that they cover many stress and strain conditions with the least amount of tests. The effective stress path of these tests in the p–q space ($p = J_1/3$ and $q = \sigma_1 - \sigma_2$) is schematically given in Fig. 8. It can be observed from the figure that the proposed tests cover a wide area of the stress space.

5.2. Consolidated drained–conventional triaxial compression stress path (CD–CTC)

Here we simulated a consolidated drained test along the conventional triaxial compression (CTC) stress path (i.e., $\Delta\sigma_1 > 0$, $\Delta\sigma_2 = \Delta\sigma_3 = 0$) using the stress to strain algorithm (Wathugala and Desai, 1994). This algorithm can be used to obtain very accurate (numerically 'exact') strain path for any stress path using HiSS models. Then the resulting strain path is given as input to all the four algorithms to obtain the corresponding stress paths. These stress paths are then compared with the original stress path to assess the accuracy of the algorithm.

Analyses were performed with very small ($\Delta\varepsilon_{\max} = 10^{-4}$ and $\text{TOL} = 10^{-5}$) to large ($\Delta\varepsilon_{\max} = 10^{-2}$ and $\text{TOL} = 1$) strain substep sizes. For small strain substeps, all the methods gave accurate and stable results. However, for large $\Delta\varepsilon_{\max}$ Implicit method moved away from the correct results and

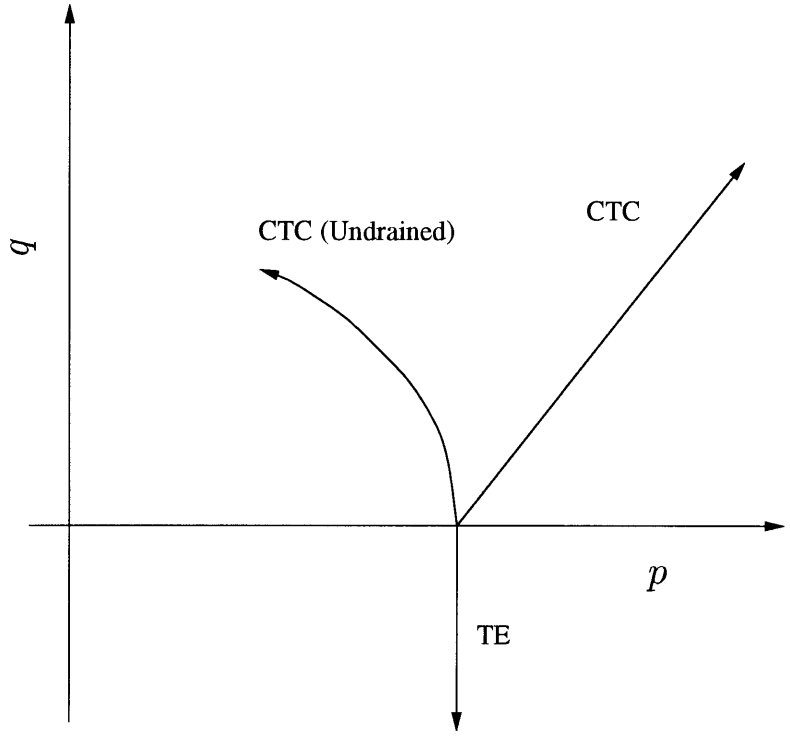

Fig. 8. Stress paths followed by different triaxial tests.

finally showed instability, as shown in Fig. 9. This was not expected since the Implicit method was claimed to be unconditionally stable (Ortiz and Popov, 1985). At present, we do not know the exact reason for this instability. However, we speculate that all the assumptions used in the proof for unconditional stability for the Implicit method may not have bene satisfied by the HiSS model. Some peculiarities of HiSS model that might contribute to this include (a) even though HiSS yield surface ($F = 0$) is convex, $F =$ constant > 0 contours near the J_1 axis are not convex. Implicit method uses the normal to these contours in its computations; (b) our definition for instability is different from that used in Ortiz and Popov (1985).

At large tolerances, stress path predicted by ME (Modified Euler) crossed the critical state line. Otherwise it provided accurate results. The performances of both EP–PC (Elastic Predictor–Plastic Corrector) and PP–PC (Plastic Predictor–Plastic Corrector) methods were similar. They predicted failure stresses accurately. However, predicted stress paths deviated a little to the right of the correct stress path.

The CPU times taken by all these analyses on a IBMRS/6000 model 355 are plotted in Fig. 10. It can be observed from here that in general Implicit method is much more computationally expensive than the other methods for this stress path. The other methods are all in the same range.

Similar trends were observed for CPU times when the same tests were run on a Pentium 150 MHz PC running Linux (Redhad 4.2) operating system with fort77 compiler.

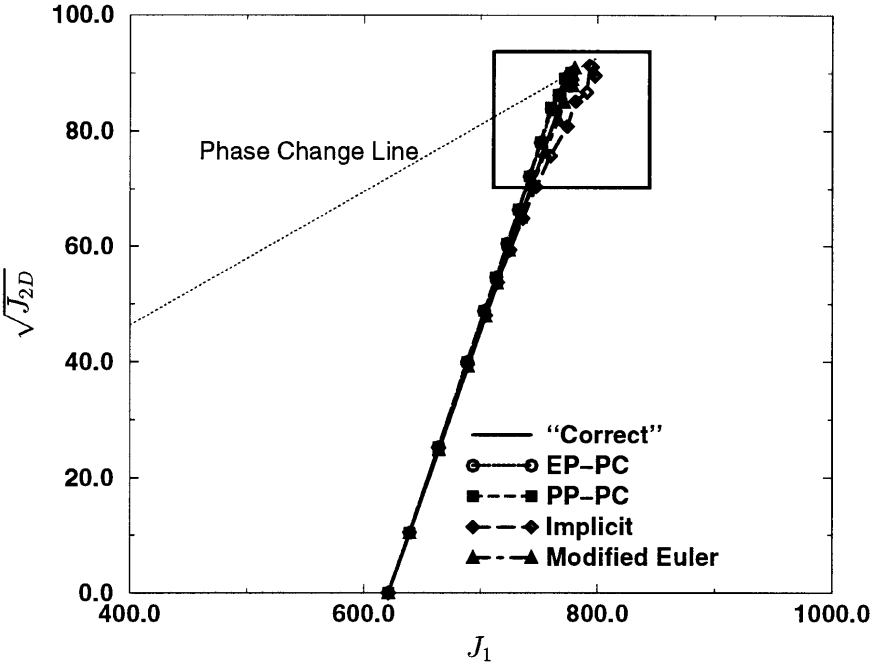

(a) Full view

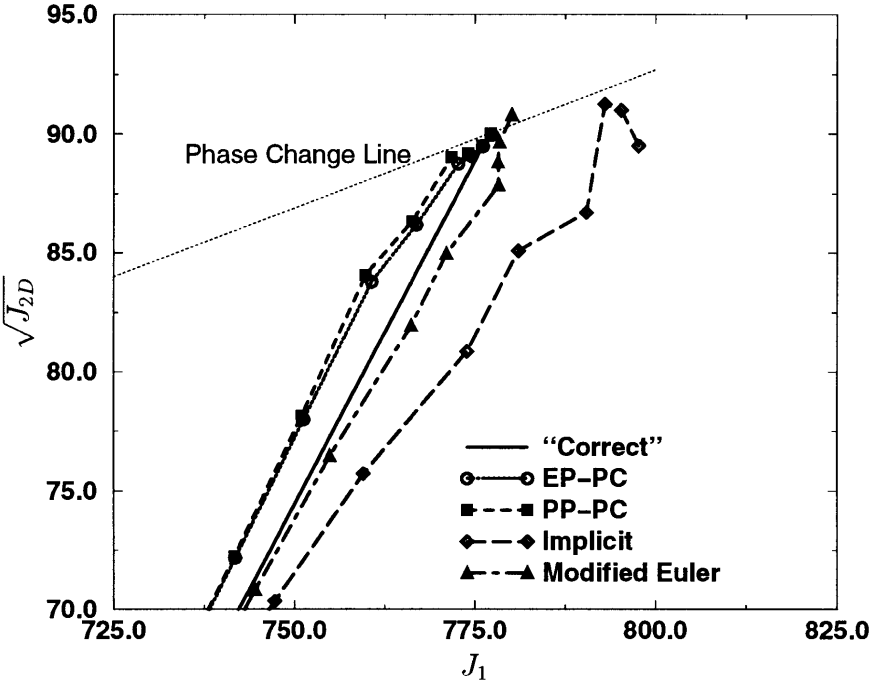

(b) Zoom view

Fig. 9. Stress paths of the CTC drained test ($\Delta\varepsilon_{max} = 10^{-2}$, TOL = 1).

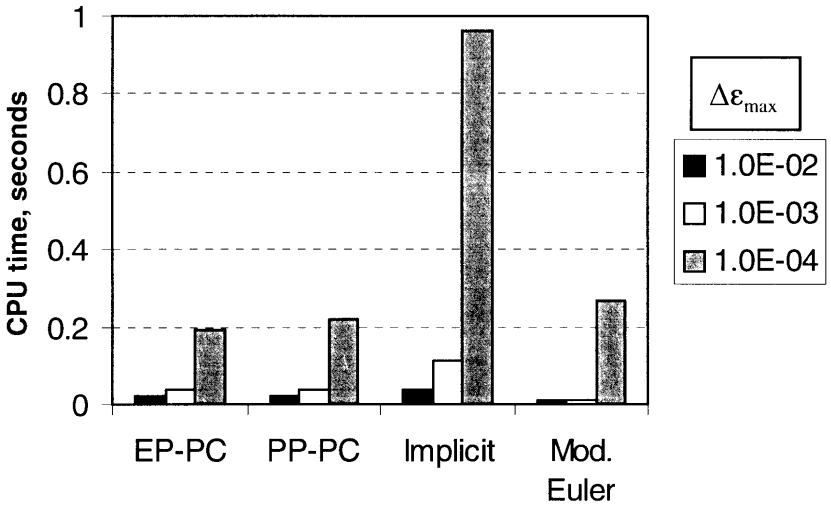

Fig. 10. CPU time taken by different algorithms for CD–CTC.

5.3. *Consolidated drained–triaxial extension* (*CD–TE*)

The same analysis procedure as for the earlier case was repeated for a CD–TE test ($\Delta\sigma_1 = -\Delta\sigma_2/2 = -\Delta\sigma_3/2 < 0$). In this case too, all the algorithms predicted identically same stress paths under small strain increments. However, it was little different from the original correct stress path for the TE test. This is due to the error induced by using a finite size strain increments to define the stress path. In subincrements, we assume that the ratio between components of the strain tensor remain constant during a strain increment. However, in the correct strain path, the ratio between strain components changes from one sub-strain increment to the next sub-strain increment. At larger strain increments, the stress paths deviated from the correct path by about 0.3%. Implicit method deviated most from the correct path. Predictions from the EP–PC and PP–PC methods moved away from the correct stress path around $\sqrt{J_{2D}} = 60$, but predicted the correct stresses at failure. All the methods were stable in this prediction.

The CPU time taken by all these analyses on an IBMRS/6000 model 355 and Pentium 150 MHz computer were compared. The same trend as in the CD–CTC case was observed here.

5.4. *Consolidated undrained–conventional triaxial compression* (*CU–CTC*)

For an undrained test on a saturated clay, volume is conserved.

$$d\varepsilon_v = d\varepsilon_1 + d\varepsilon_2 + d\varepsilon_3 = 0. \tag{19}$$

For isotropic samples on the axisymmetric loading from the triaxial equipment $d\varepsilon_2 = d\varepsilon_3$. Therefore, this test can be simulated as a strain controlled test by applying $d\varepsilon_1 = -2d\varepsilon_2 = -2d\varepsilon_3$. As in the earlier cases, all the methods predicted the same stress path for small strain increments. Therefore, we denoted that path as the 'correct' stress path. Even for large strain increments, all

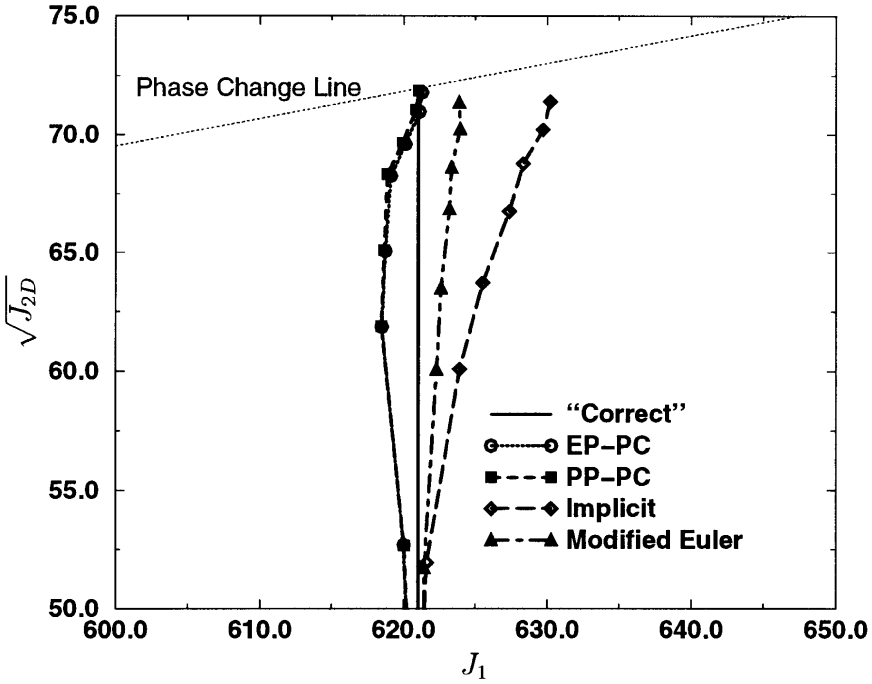

Fig. 11. Stress paths of the TE drained test ($\Delta\varepsilon_{max} = 10^{-2}$, TOL = 1).

the algorithms predicted accurate stress paths. However, as in CD–CTC, predicted stress path for ME crossed the critical state line and Implicit method became unstable near failure (Fig. 12).

The CPU time taken by all these analyses on an IBMRS/6000 model 355 and on a Pentium 150 MHz PC were compared. The same trend as in the other two cases was observed here.

5.5. Finite element simulations

All the algorithms have been implemented in the commercial finite element program, ABAQUS (HKS, Inc., 1997). In this section, we present results of comparison of finite element simulations of strip footings on the same clay soil used in earlier triaxial test simulations with all the four algorithms. Both rigid, displacement controlled and flexible, load controlled footings were analysed. The finite element mesh for both problems is the same and is given in Fig. 13. All the elements are eight noded plain strain isoparametric elements with reduced integration (Element type CPE8R in ABAQUS). The number of elements were made small in order to facilitate the large number of analyses in the study. Initial conditions such as stresses, and hardening parameters were computed by assuming normally consolidated clay at K_0 (= 0.52) stress conditions. In order to minimize numerical problems due to zero effective stress state on the surface, a surcharge of 20 kPa was applied on the surface of the clay for all the problems. This may be interpreted as a soil of about 1 m deep without any shear strength. Sometimes it is necessary to develop special procedures to handle stress points $J_1 = 0$ efficiently. Therefore, it was decided to add this surcharge so that this aspect will not interfere with our comparisons.

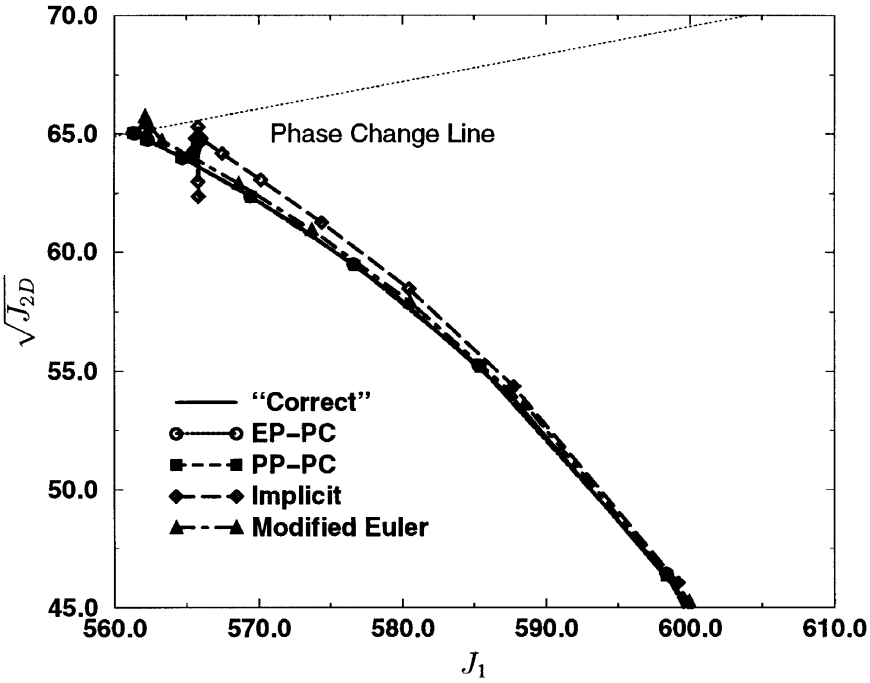

Fig. 12. Stress paths of the CTC undrained test ($\Delta\varepsilon_{max} = 10^{-2}$, TOL = 1).

5.6. Rigid footing

Here, all the nodes under the footing were given the same vertical displacement until failure of the footing. Two hundred equal displacement increments of 0.4 mm each were applied. The problem was analysed with different $\Delta\varepsilon_{max}$ for EP–PC, PP–PC and Implicit methods and different tolerance for the ME method. For very small $\Delta\varepsilon_{max}$ ($<10^{-4}$) EP–PC, PP–PC and Implicit methods gave the same load deformation curve, as shown in Fig. 14. However, ME with very small tolerances (i.e., TOL $< 10^{-5}$) differed near failure, as shown in Fig. 14. To investigate these unexpected results, we performed an analysis with 1200 small increments of 0.067 mm displacement using ME method. However, still it did not converge to the solution obtained from the other methods. At this point, we computed the values of F, stress ratio ($\sqrt{J_{2D}}/J_1$) and the distance from the yield surface for all the Gauss integration points at failure for EP–PC and ME methods. For the EP–PC method, results indicated that stress points were on the yield surface or inside it as expected. However, in the ME method, for several Gauss points, stress points were far outside the current yield surface. This is due to the accumulation of errors in each small step. Readers may recall that in the ME method, we do not perform any drift correction. Therefore, it was concluded that the converged results obtained from other methods are the 'correct' solution for the footing problem. This result was denoted as the 'correct' solution for the problem in subsequent analyses with larger $\Delta\varepsilon_{max}$ and TOL. ME method failed to achieve convergence for higher tolerances ($>10^{-5}$). The other three methods provided accurate and stable results for all the $\Delta\varepsilon_{max}$ values (i.e., 10^{-2}, 10^{-3} and 10^{-4}).

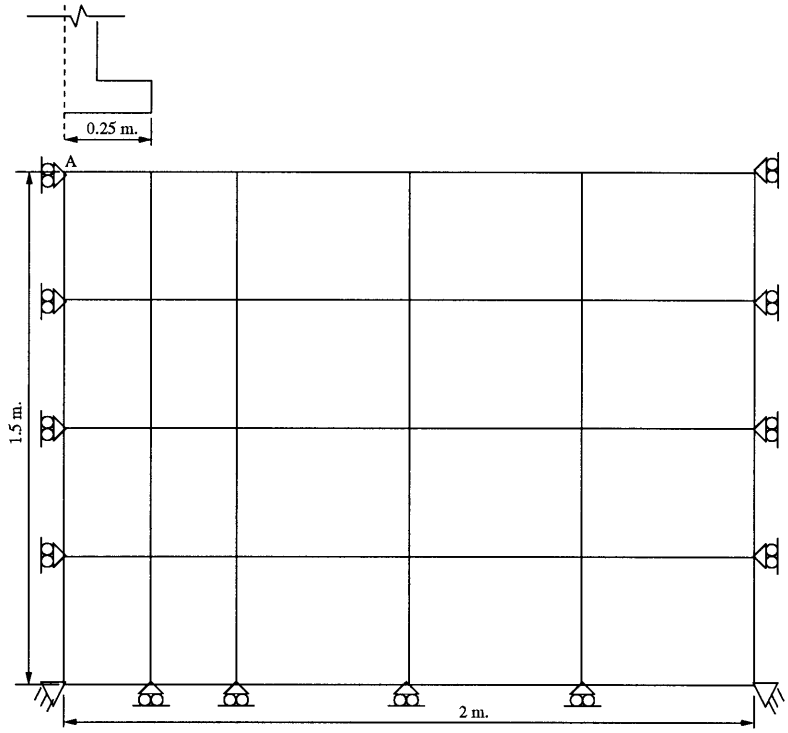

Fig. 13. FEM mesh for the footing problem.

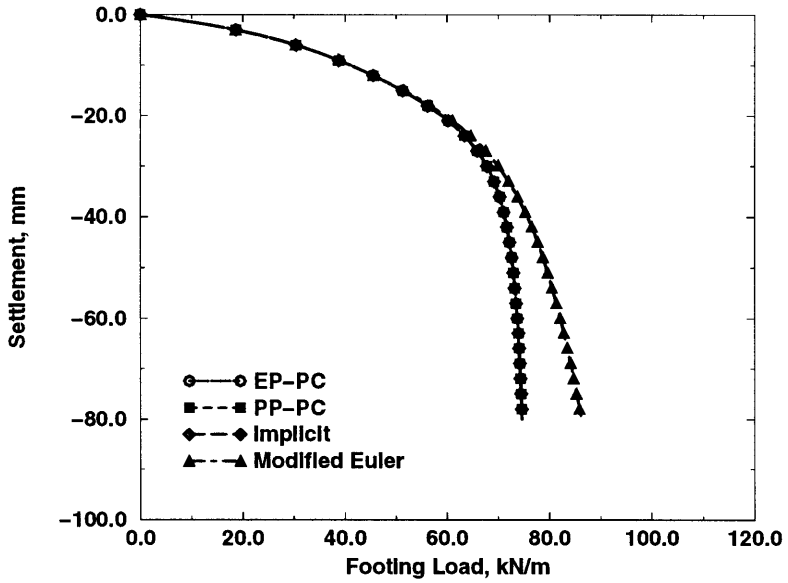

Fig. 14. Load-settlement curves for the rigid footing ($\Delta\varepsilon_{\max} = 10^{-4}$, TOL $= 10^{-5}$).

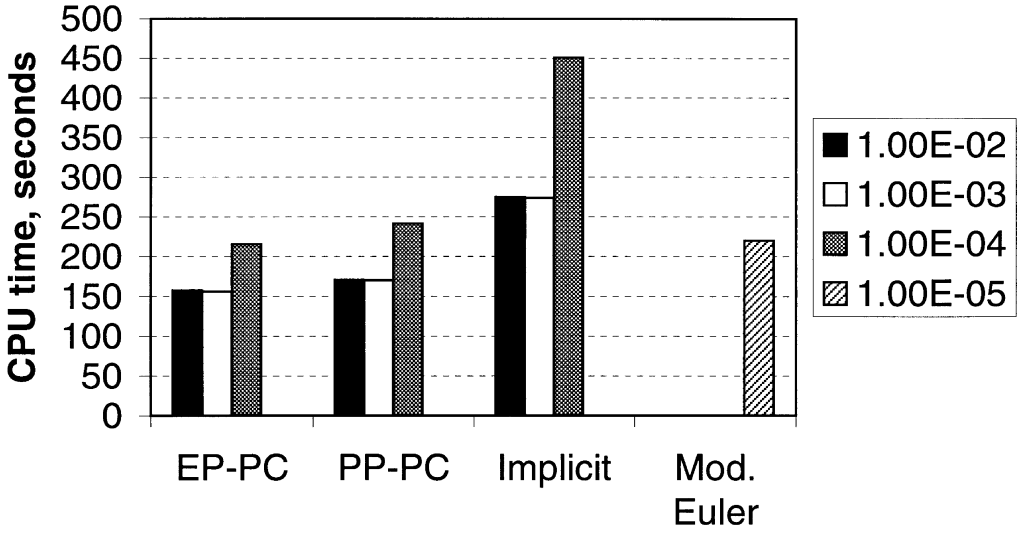

Fig. 15. CPU time taken by different algorithms for the rigid footing.

Figure 15 shows the CPU time taken by each analysis on an IBMRS/6000 Model 355 workstation. Maximum strain step size for each analysis is given in the legend for all the methods except ME. For ME, TOL value is given in the legend. Similar trends as for the triaxial stress paths have been observed here. The Implicit method is the most expensive one in terms of CPU time. For given accuracy and stability, EP–PC and PP–PC are the least CPU time-consuming.

5.7. *Flexible footing*

Here, 135 kPa footing pressure was applied in 135 equal increments. Figure 16 compares the load settlement curves for all the algorithms with small strain increments (i.e., $\Delta\varepsilon_{max} < 10^{-4}$ for EP–PC, PP–PC and Implicit and TOL $< 10^{-5}$ for ME). As in the case with the rigid footing, EP–PC, PP–PC and Implicit methods converged to the same load settlement curve for small $\Delta\varepsilon_{max}$. However, converged solution for the ME differed from the other methods even for small tolerances. After investigating, it was found that the stress state at some Gauss integration points in the ME method were outside the yield surface. Therefore, the converged solution from the first three methods was denoted as 'correct' solution for this problem too. For large $\Delta\varepsilon_{max}$ values, Implicit method did not converge at around 25 mm of settlement. EP–PC and PP–PC methods converged for all the strain step sizes.

Similar trends for CPU time as for the triaxial stress paths and the rigid footing have been observed here. The Implicit method is the most expensive one in terms of CPU time. For given accuracy and stability, EP–PC and PP–PC are the least CPU time-consuming.

6. Conclusions

Four different algorithms: (a) Elastic Predictor–Plastic Corrector (EP–PC), (b) Plastic Predictor–Plastic Corrector (PP–PC), (c) Backward Euler or Implicit and Modified Euler (ME) for implemen-

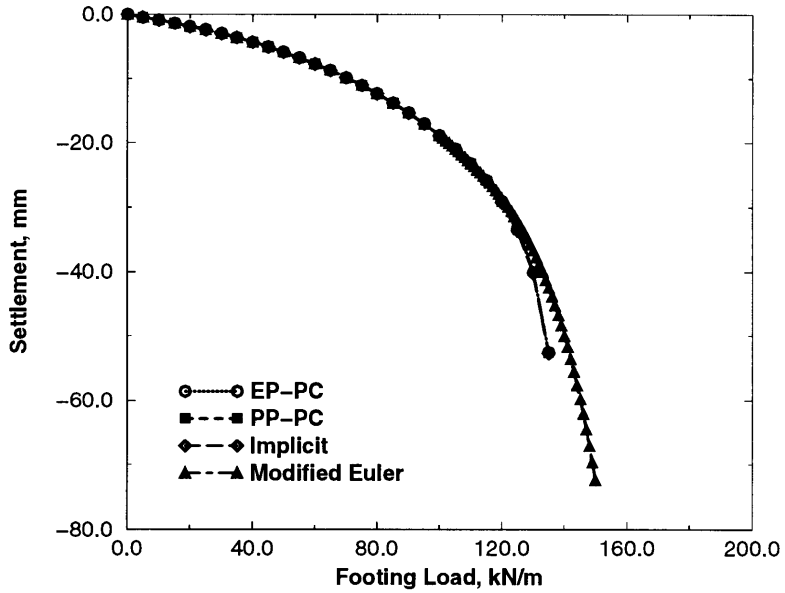

Fig. 16. Load-settlement curves for the flexible footing ($\Delta\varepsilon_{max} = 10^{-4}$, TOL $= 10^{-5}$).

tation of plasticity based constitutive models under virgin loading were reviewed. All these algorithms were implemented in the commercial finite element program ABAQUS. Relative performance in terms of accuracy, stability and efficiency of these four algorithms in simulating laboratory triaxial tests in a variety of stress paths and load controlled and displacement controlled strip footings was compared.

6.1. Accuracy

For the triaxial stress paths, all the algorithms gave accurate results with small strain increments. EP–PC, PP–PC and Modified Euler produced more accurate results than Implicit method for large strain increments. However, for some tests, ME predicted stress path passed the critical state line. EP–PC, PP–PC and Implicit methods produced accurate results for the finite element analysis of both rigid and flexible footings. Modified Euler method predicted failure loads higher than the other methods possibly due to its inability to satisfy consistency condition at all the Gauss integration points.

6.2. Stability

All the algorithms were stable with small strain increments for simple stress paths. EP–PC, PP–PC and Modified Euler were stable even for large strain increments. Implicit method became unstable near failure for large strain increments. This was not expected because the Implicit Method is known to be unconditionally stable (Ortiz and Popov, 1985). However, the definition of instability here is qualitative and is different from Ortiz and Popov (1985). The nonconvex contours of $F =$ constant > 0 near $J_1 = 0$ may have contributed to this instability. In general, it

was found that the Finite element analysis of the displacement controlled rigid footing was more stable than the load controlled flexible footing. For smaller strain increments all the methods were stable. However, for large strain increments, Modified Euler method became unstable for both footing problems. For large strain increments, Implicit method was stable for the rigid footing but not for the flexible footing. EP–PC, PP–PC were stable for large increments for both footings.

6.3. *Efficiency*

EP–PC, PP–PC and Modified Euler methods were more efficient than Implicit method for simple stress paths. In finite element analyses, EP–PC, PP–PC were more efficient than ME and Implicit method.

Based on the systematic numerical analyses presented here, it can be concluded that EP–PC, PP–PC both perform equally well in all the aspects. Even though only the HiSS δ_0^* was used in the present study, the results obtained here could provide useful insights for other elasto-plastic models in use for soils.

Acknowledgements

Financial support from National Science Foundation Research Initiation Award No. CMS 9410482, Louisiana Board of Regents grant Nos LEQSF (1994–97)-RD-A-08, and LEQSF (1994–96)-ENH-TR-28 and Louisiana Transportation Research Center, are gratefully acknowledged.

References

Borja, R.I., Lee, S.R., 1990. Cam-clay plasticity: implicit integration of elasto-plastic constitutive relations. Computer Methods in Applied Mechanics and Engineering 78, 49–72.

Faruque, M.O., Desai, C.S., 1985. Implementation of a general constitutive model for geologic materials. J. Numer. Analyt. Meth. Geomech. 9, 415–436.

Ganendra, D., Potts, D.M., 1994. A comparison between explicit and implicit stress point algorithms. In: Siriwardene, Zaman (Eds.). Computer Methods and Advances in Geomechanics. A.A. Balkema, Rotterdam, The Netherlands, pp. 1975–1980.

HKS, Inc., 1997. ABAQUS/Standard User's Manual, vol. I–II, version 5.6. Hibbit, Karlsson & Sorensen, Inc., Pawtucket, Rhode Island.

Jeremic, B., Sture, S., 1995. Implicit integration in geoplasticity. Proceedings of the 10th Engineering Mechanics Conference, ASCE, Boulder, Colorado, pp. 1099–1102.

Macari, E.J., Weihe, S., Arduino, P., 1997. Implicit integration of elastoplastic constitutive models for frictional materials with highly non-linear hardening functions. Mechanics of Cohesive-Frictional Materials 2, 1–29.

Nayak, G.C., Zienkiewicz, O.C., 1972. Elasto-plastic stress analysis: a generalization for various constitutive laws including strain softening. Int. J. Numer. Meth. Eng. 5, 113–135.

Ortiz, M., Popov, E.P., 1985. Accuracy and stability of integration algorithms for elasticplastic constitutive relations. Int. J. Numer. Meth. Eng. 21, 1561–1576.

Ortiz, M., Simo, J.C., 1986. An Analysis of a New Class of Integration Algorithms for Elastoplastic constitutive Relations. Int. J. Numer. Meth. Eng. 23, 353–366.

Pal, S., 1997. Numerical simulation of geosynthetic reinforced earth structures. Ph.D. Dissertation, Louisiana State University, Baton Rouge, U.S.A.

Potts, D.M., Gens, A., 1985. A critical assessment of methods of correction for drift from the yield surface in elasto-plastic finite element analysis. Int. J. Num. Analyt. Meth. Geomech. 6, 149–159.

Simo, J.C., Taylor, R.L., 1985. Consistent tangent operators for rate-independent elastoplasticity. Computer Methods in Applied Mechanics and Engineering 48, 101–118.

Sloan, S.W., 1987. Substepping schemes for the numerical integration of elastoplastic stress-strain relation. Int. J. Numer. Meth. Eng. 24, 893–911.

Wathugala, G.W., 1990. Finite element dynamic analysis of nonlinear porous media with applications to piles in saturated clays. Ph.D. Dissertation, University of Arizona, Tucson, Arizona.

Wathugala, G.W., Desai, C.S., 1991a. Hierarchical single surface model for isotropic hardening cohesive soils. In: Desai et al. (Eds.). Constitutive Laws for Engineering Materials: Recent Advances and Industrial and infrastructure Applications. ASME Press, New York, pp. 231–234.

Wathugala, G.W., Desai, C.S., 1991b. Hierarchical Single Surface Model for Anisotropic Hardening Cohesive Soil. In: Beer, J., Booker, J.R., Carter, J.P. (Eds.). Computer Methods and Advances in Geomechanics: Proceedings of the 7th Int. Conf. of the International Association for Computer Methods and Advances in Geomechanics, May 6–10, Cairns, Australia; A.A. Balkema, Rotterdam, The Netherlands, pp. 1249–1254.

Wathugala, G.W., Desai, C.S., 1993. Constitutive model for cyclic behavior of clay I: Theory. Journal of Geotechnical Engineering, ASCE 119 (4) 714–729.

Wathugala, G.W., Desai, C.S., 1994. Stress to strain algorithm for HiSS models. In: Siriwardene, H.J., Zaman, M.M. (Eds.). Computer Methods and Advances in Geomechanics: Proceedings of the 8th Int. Conf. of the International Association for Computer Methods and Advances in Geomechanics, May 22–28, Morgantown, U.S.A.; A.A. Balkema, Rotterdam, The Netherlands, pp. 725–729.

Wathugala, G.W., Pal, S., 1996. Improving robustness of algorithms to implement HiSS models in FEM. Proceedings of the 11th Engineering Mechanics Conference, ASCE, Fort Lauderdale, Florida, U.S.A., May 19–22, pp. 144–147.